Detection of Boundary Layer Water Clouds by Spaceborne Cloud Radar

R. BAEDI

IRCTR, Delft University of Technology, Delft, Netherlands

R. BOERS

CSIRO Atmospheric Research, Aspendale, Victoria, Australia

H. RUSSCHENBERG

IRCTR, Delft University of Technology, Delft, Netherlands

(Manuscript received 24 August 2001, in final form 20 February 2002)

ABSTRACT

A model for the radar reflectivity of boundary layer water clouds is constructed using cloud droplet spectra fitted to a truncated gamma distribution. The spectra were derived from several recent field experiments. Realistic space-based radar returns are simulated that take into account the pulse shape, digitization interval, averaging volume, and variations in droplet concentration, cloud depth, and cloud-top height. The results show that the long pulse length of the proposed radar is responsible for smearing out the real reflectivity spatially so that the space-based detected clouds occupy a volume far exceeding that of the ''observed'' cloud. However, the effect of smearing is reduced by the limited receiver sensitivity. Cloud volume of boundary layer clouds is overestimated by between 30% and 100% using proposed radar parameters. Even if clouds are detected, the radar reflectivity convoluted by the pulse shape is sufficiently different from the originally observed reflectivity to seriously impede the retrieval of accurate cloud liquid water content.

1. Introduction

A precise assessment of the importance of clouds in the earth radiation budget relies on knowledge of cloud cover, cloud thickness, and cloud microphysical properties. While a combination of ground-based passive and active instruments have been used to develop methods for cloud detecting (e.g., Boers et al. 2000), global-scale information about clouds can be obtained only by space-based instruments. Space-borne passive instruments have been used to derive cloud-top temperature and coverage as well as integrated cloud parameters such as the optical depth and the liquid water path. The best example of such an integrated dataset on cloud cover is provided by the International Satellite Cloud Climatology Project (ISCCP; Rossow and Schiffer 1991; Rossow and Garder 1993; Han et al. 1994; Lin and Rossow 1994).

To gather information about the vertical structure of clouds, several meteorological satellites utilizing active instruments will be launched in the next few years. Theoretically, spaceborne radar would be capable of collecting information about the cloud thickness and the altitude of clouds on a global scale. Also, spaceborne radar would be capable of retrieving cloud parameters such as the effective radius and the liquid water mixing ratio on a global scale using a set of simple assumptions. In the absence of real spaceborne radar data it is at present difficult to gauge precisely the utility of expected radar returns, although some investigators (Fox and Illingworth 1997a,b) have attempted to predict the radar signal strength based on collections of aircraft data. In particular, Fox and Illingworth (1997a) discussed boundary layer clouds and the impact of drizzle on spaceborne radar returns. Their study concludes that for a sensitivity of -30 dBZ, radar would detect around 85% of drizzling marine boundary layer clouds but only 33% of nondrizzling continental clouds. Unfortunately, the effect of drizzle is to break the straightforward link between radar reflectivity and liquid water, so that its occurrence greatly restricts the investigator in assigning unambiguously microphysical parameters to spaceborne cloud observations.

The purpose of this paper is to further explore boundary layer cloud detection by space-borne radar. A simple model of cloud reflectivity will be constructed that is a function of the droplet concentration and cloud liquid water content. This model is used to construct a uni-

Corresponding author address: Reinout Boers, KNMI, P.O. Box 301, 3730AE De Bilt, Netherlands.
E-mail: boers@knmi.nl

versal diagram that can be used to assess the possibility of spaceborne radar detection of boundary layer cloud given cloud depth, droplet concentration, and/or liquid water content. Model construction necessitates the use of a model for the droplet size distribution. A truncated gamma distribution is used because the transformation to drizzle droplets occurs abruptly at droplet radii exceeding 20 μm, and because the tail end of a complete gamma distribution has an unacceptably large contribution to the total radar reflectivity, which is proportional to the sixth power of the droplet radius.

The parameters describing the gamma distribution were estimated using in situ probe measurements collected during the Southern Ocean Cloud Experiment (SOCEX), the Cloud Lidar And Radar Experiment 1998 (CLARE98; ESA 1999), and several research flights conducted off the Namibian coast. During SOCEX (Boers et al. 1996, 1998) droplet concentrations were observed that are among the lowest ever recorded (15–30 cm^{-3}), and we will show that they are responsible for the highest radar reflectivity for nondrizzling clouds that can realistically be expected. CLARE98 data reflect typical Northern Hemisphere conditions. Using the gamma distribution parameters a cloud reflectivity model is constructed, and the expected spaceborne radar signal is simulated by convoluting the ''actual'' reflectivity with the radar signal. The impact of the large radar resolution volume on the performance of the radar to map the cloud stratification is discussed with the aid of a fractal model, which simulates a cloud with a horizontal extent of about 25 km $\times$ 25 km; the fractal model represents the spatial structure of typical boundary clouds.

2. Theory

a. The truncated gamma distribution

Cloud spectra are often bimodal, one mode associated with suspended cloud droplets, the other with drizzle droplets. Both modes can, in principle, be modeled by a three-parameter gamma distribution (see, e.g., Clothiaux et al. 1995).

$$n(r, z) = a(z)r^{\alpha(z)} \exp[-b(z)r], \tag{1}$$

where r is the particle radius, a is a scaling parameter, α is the shape parameter, and b determines the skewness of the distribution; z represent altitude above cloud base. Cloud droplets with radius larger than about 20 μm rapidly become susceptible to collision-coalescence processes, which results in falling drizzle droplets. The tail of the complete gamma distribution therefore overestimates the number of large suspended droplets. While potential errors are small when simulating the zeroth (concentration), second (optical depth), or third moment (liquid water content), the radar reflectivity is proportional to the sixth moment of the radius, so that a sizable portion of the calculated reflectivity may be due to the nonexistent particles in the tail of the modeled distribution. Therefore, as an alternative we decided to use a truncated gamma function for the suspended cloud droplet spectra (i.e., nondrizzle), which integrates the particle spectrum up to the maximum particle radius measured by the Forward Scattering Spectrometer Probe (FSSP), $r_{\max}$. The FSSP is the instrument of choice to measure cloud droplets, while the 2DC probe images the larger drizzle droplets. The complete gamma function can however be used for the drizzle mode: the tail of the distribution represents the drizzle particles, and yet approaches zero fast enough to exclude large raindrops from the distribution.

The full expressions for the droplet concentration N_T, the liquid water mixing ratio l, and the reflectivity Z for nondrizzling clouds (assuming Rayleigh scattering, which is still valid at the proposed radar frequency of 94 GHz) can be written as

$$\begin{aligned} N_T(z) &= \int_0^{r_{\max}} n(r, z)\, dr \\ &= a(z)b(z)^{-[\alpha(z)+1]}\Gamma[\alpha(z) + 1]P[\alpha(z) + 1] \end{aligned} \tag{2}$$

$$\begin{aligned} l(z) &= \frac{4\pi\rho_w}{3\rho_o} \int_0^{r_{\max}} n(r, z)r^3\, dr \\ &= \frac{4\pi\rho_w}{3\rho_o} a(z)b(z)^{-[\alpha(z)+4]}\Gamma[\alpha(z) + 4]P[\alpha(z) + 4] \end{aligned} \tag{3}$$

$$\begin{aligned} Z(z) &= 64 \int_0^{r_{\max}} n(r, z)r^6\, dr \\ &= 64a(z)b(z)^{-[\alpha(z)+7]}\Gamma[\alpha(z) + 7]P[\alpha(z) + 7], \end{aligned} \tag{4}$$

where ρ_w is the density of liquid water, ρ_o is the density of dry air, $\Gamma(\alpha)$ is the gamma function, and the P factor is defined as

$$P[\alpha(z) + i] = \frac{\displaystyle\int_0^{r_{\max}\cdot b(z)} r'^{\alpha(z)+i-1} \exp(-r')\, dr'}{\displaystyle\int_0^{\infty} r'^{\alpha(z)+i-1} \exp(-r')\, dr'}. \tag{5}$$

The three shape parameters α, a, and b can be determined from (2) to (4) using individually measured size spectra by calculating N_T, l, and Z while integrating over the spectral bins and solving the three transcendental equations for the three unknowns. The effective radius r_e is a derived parameter, and is defined as the ratio of the third moment and the second moment of the droplet distribution:

$$r_e(z) = \frac{\int_0^{r_{\max}} n(r, z) r^3 \, dr}{\int_0^{r_{\max}} n(r, z) r^2 \, dr} = b(z)^{-1}[\alpha(z) + 3]\frac{P[\alpha(z) + 4]}{P[\alpha(z) + 3]}, \quad (6)$$

while the optical depth is given by

$$\tau(z) = \pi Q_{\text{ext}} \int_{z_b}^{z} \int_0^{r_{\max}} n(r, z) r^2 \, dr \, dz = \pi Q_{\text{ext}} \int_{z_b}^{z} a(z) b(z)^{-[\alpha(z)+3]} \Gamma[\alpha(z) + 3] \times P[\alpha(z) + 3] \, dz, \quad (7)$$

where z_b is cloud-base height and Q_{ext} is the extinction efficiency ($\sim$2).

In the case of drizzle Eq. (2)–(6) are used as well, but the *P*-correction factors are disregarded, which means that we resort to the complete gamma function.

b. Size distribution moments and universal links to cloud depth and cloud optical depth

It is instructive to examine some universal links between the various moments of the droplet spectrum and the cloud optical depth. In case the cloud is not contaminated by drizzle, it may be assumed that the liquid water mixing ratio varies linearly with height (Boers and Mitchell 1994):

$$l(z) = (1 - \beta) A_d (z - z_b), \quad (8)$$

where A_d is the vertical gradient of the adiabatic liquid water mixing ratio, and β is a mixing parameter denoting the departure from the adiabatic state (Betts 1982).

Using the simplifying assumption that the total droplet concentration N_T and α are constant with height, then the substitution of (2), (3), and (8) into (7) yields an optical depth of

$$\tau_z = \frac{6}{5}\pi^{1/3} l(z)^{5/3}[(1 - \beta)A_d]^{-1} \psi_1 \left[\frac{4\rho_w P(\alpha + 4)}{3\rho_0 P(\alpha + 1)}\right]^{-2/3} \times \frac{P(\alpha + 3)}{P(\alpha + 1)} N_T^{1/3}, \quad (9)$$

where $\Gamma(\alpha)$ has been replaced by $(\alpha - 1)!$ and $\psi_1 = \{[(\alpha + 1)(\alpha + 2)]/[(\alpha + 3)^2]\}^{1/3}$.

Similarly, the expressions for the effective radius and the reflectivity can also be written in terms of $l(z)$ and N_T:

$$r_e(z) = l(z)^{1/3} \psi_1^{-1} \left[\frac{4\pi\rho_w P(\alpha + 4)}{3\rho_0 P(\alpha + 1)}\right]^{-1/3} \times \frac{P(\alpha + 4)}{P(\alpha + 3)} N_T^{-1/3} \quad (10)$$

$$Z(z) = 64 l(z)^2 \psi_2 \left[\frac{4\pi\rho_w P(\alpha + 4)}{3\rho_0 P(\alpha + 1)}\right]^{-2} \frac{P(\alpha + 7)}{P(\alpha + 1)} N_T^{-1}, \quad (11)$$

where $\psi_2 = [(\alpha + 6)(\alpha + 4)(\alpha + 5)]/[(\alpha + 3)(\alpha + 2)(\alpha + 1)]$. Z has the dimension m^3, but is usually expressed in $\text{mm}^6\ \text{m}^{-3}$ or its logarithmic equivalent dBZ; 0 dBZ corresponds to 1 $\text{mm}^6\ \text{m}^{-3}$. The dimension of $r_e(z)$ is m; because of the small size of cloud droplets the unit μm is used in this paper. The mixing ratio $l(z)$ is dimensionless. Here N_T is the number of particles per unit of volume; in this paper cm^{-3}. The optical thickness is dimensionless. In this paper, $r_{\max}$ is set to 23 μm. The reflectivity is thus a quadratic function of height, and inversely proportional to N_T. This implies that, all other factors being equal, the reflectivity in the Northern Hemisphere will generally be lower than in the Southern Hemisphere because industrial sources of air pollution and thus cloud condensation nuclei are more abundant in the Northern Hemisphere than in the Southern Hemisphere. During the SOCEX in situ observations were made of marine stratiform clouds located west of Tasmania (Boers et al. 1996, 1998). This region is subjected to an extremely low concentration of anthropogenic cloud condensation nuclei, resulting in droplet concentrations that are among the lowest in the world. Equation (11) indicates that the data from SOCEX would generate the highest reflectivities, all other factors being equal. Equation (11) also suggests the well-known possibility to retrieve liquid water content from cloud reflectivity, provided N_T is derived from other sources.

c. Application to in situ data

As mentioned, the three parameters describing the gamma function may be estimated using Eq. (2)–(4), where the values of N_T, l, and Z are those computed from the in situ measured droplet concentrations. Table 1 contains the mean values of the three parameters of the truncated gamma distribution. The values are obtained using the in situ data collected during SOCEX 1 and SOCEX 2. All data were taken using the same probes. Data reflect level flight legs at various altitudes inside clouds and correspond to scales from 5 up to 20 km. So, the smallest scales are comparible to those of the volume-averaged radar reflectivity but can, for longer averaging time, be larger by a factor of three to four as we will see below.

For comparison, the results for CLARE98, which was held over Chilbolton (United Kingdom), and some research flights conducted off the Namibian coast, are given as well (courtesy P. Francis, Met Office). For all campaigns, the in situ measured particle size distribu-

TABLE 1. Mean parameters for the (in)complete gamma distribution derived from several field experiments.

	α	a	b	N_T (cm^{-3})	l (g kg^{-1})	R_e (μm)	Z (dBZ)
FSSP							
SOCEX1	10.39	0.010	1.16	2.18–70.13 (19.84)	0.072	11.91	−24.48
SOCEX2	9.51	0.12	1.41	3.64–122.30 (56.21)	0.10	9.14	−26.32
CLARE	6.63	1.18	1.16	15.35–412.31 (115.98)	0.14	8.36	−25.42
Namibia	13.99	1.14	2.20	99.04–158.87 (127.55)	0.15	7.40	−27.11
2DC							
SOCEX1	1.01	5.05e-5	0.026	0.015	0.14	200.74	23.45
SOCEX2	1.79	6.87e-5	0.042	0.027	0.094	123.19	16.81
CLARE	0.026	0.0028	0.033	0.066	0.026	106.60	7.17
Namibia	N/a	N/a	N/a	0.012	0.0012	34.12	−25.50

tions are averaged over the length of an entire flight, which is about 10–30 min. Table 1 contains the average value of the cloud parameters encountered during the four experiments. For the total droplet concentration in the nondrizzle case, the range of measured values is given as well. When compared to the truncated gamma distribution, the nonexistent tail of the complete gamma distribution contributes up to 30% to the total reflectivity. Thus, it is essential to use the truncated gamma function in order to make proper estimates of the distribution's parameters.

The estimated gamma parameters can now be used to construct a diagram of l vs N_T, with isolines of the effective radius, reflectivity, and optical depth [Eq. (9)–(11)]. To obtain the optical depth and height above cloud base the additional two assumptions are that $\beta = 0.4$ and that N_T and α are constant with height. The parameter β reflects the fact that clouds are rarely adiabatic; the value of 0.4 follows from a ground-based remote sensing experiment during the Clouds And Radiation experiment (CLARA) campaigns in 1996 in the Netherlands (Boers et al. 2000). In that experiment it was shown that β may vary between 0.2 and 0.6 for a closed stratocumulus field.

The purpose of Fig. 1 is to visualize the link between the cloud parameters and their vertical variation in the nondrizzle case, and provides a clear picture of the expected reflectivity, mean particle size, and optical depth given that the liquid water mixing ratio and the total droplet concentration are known. In other words, the

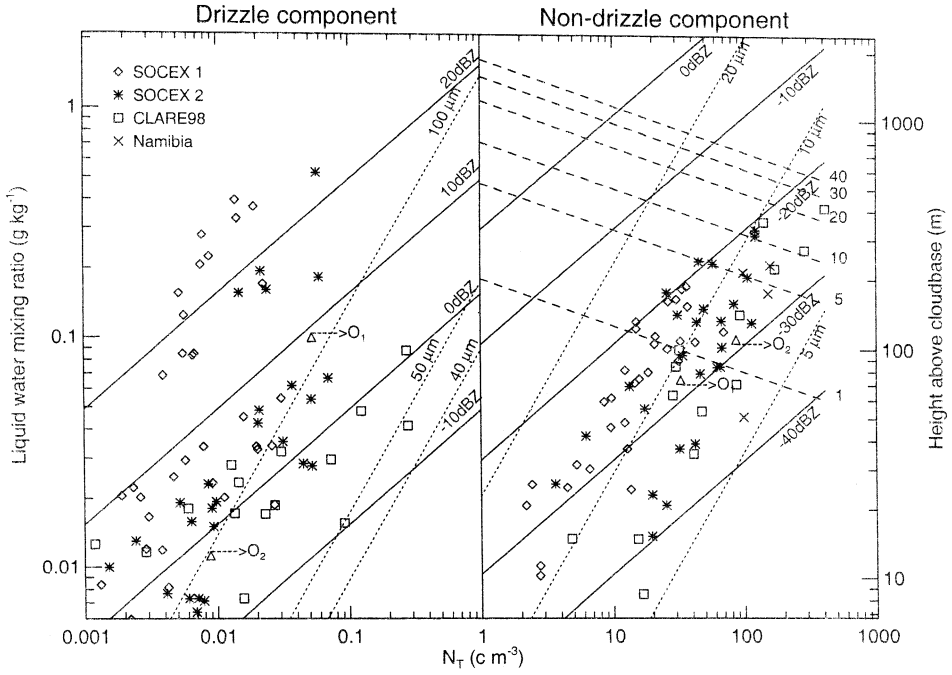

FIG. 1. The link between cloud droplet concentration, liquid water content, radar reflectivity, optical depth, effective radius, and height above cloud base. The model linking these parameters uses a truncated gamma distribution for the nondrizzle component and a complete gamma distribution for the drizzle component of the cloud droplet spectra. The points in the plot are based on the four experiments indicated in the legend, where individual flight legs have been averaged over 15–30 min.

diagram provides an estimate of three cloud parameters given that two other parameters are known. Clearly, this figure is only an estimate based on only a few experiments and is therefore valid only as a guide to expected behavior. The right-hand side of Fig. 1 represents the nondrizzle component of the particle spectra where $\alpha = 9.93$ (average α over SOCEX1 and SOCEX2), whereas the left-hand side is the drizzle component where $\alpha = 1.39$. Notice that the optical depth, as represented by Eq. (9), is only valid for the nondrizzle case, where it may be assumed that the liquid water mixing ratio varies linearly with height. Therefore, its isolines are omitted from the left side of the figure.

To illustrate the universal character of this diagram, if $N_T = 300$ cm^{-3} and assuming a cloud depth of 200 m, then the radar reflectivity is expected to be around -30 dBZ at the cloud top (and decreasing below cloud top), while the cloud optical depth would be about 8. When $N_T = 50$ cm^{-3}, however, a cloud of the same depth would have a reflectivity of -22 dBZ near cloud top and an optical depth of roughly 5. This is an important result as it directly visualizes the restrictions on cloud detection by the spaceborne radar. It implies that a typical sensitivity of -30 dBZ for cloud radar would not be sufficient to detect many continental clouds. On the other hand, increasing the sensitivity to -40 dBZ would greatly improve the detectability of continental clouds. The in situ–based values are in line with the actual radar observations described in Clothiaux et al. 1995.

The in situ probe data from SOCEX1, SOCEX2, CLARE98, and Namibia (diamonds, asterisks, squares, and crosses, respectively, plotted as l vs N_T) are superimposed on the figure to illustrate the contribution of the drizzle component to the total reflectivity. The scatter in the diagram for a given N_T is not in disagreement with what could be expected due to adiabatic variation, assuming that β varies between 0.2 and 0.6. Two examples are considered. In the first example the nondrizzle component contains a total number of droplets of 33 cm^{-3}, while in the second example this number is 87 cm^{-3}. First, consider the observation O_1 marked with a triangle. The nondrizzle component ($N_T = 33$ cm^{-3}, $l = 0.066$ g kg^{-1}, $r_e = 9.84$ μm, as computed from the in situ measured particle spectra) has a reflectivity of -27.23 dBZ. Its associated drizzle component ($N_T = 0.053$ cm^{-3}, $l = 0.099$ g kg^{-1}, $r_e = 105.51$ μm) has a reflectivity of 8.11 dBZ and thus dominates the total reflectivity. In this case, the contribution of the drizzle component to the total liquid water mixing ratio is also significant (60.19%). For observation O_2, the total concentration of the nondrizzle component is 87 cm^{-3}, with a liquid water mixing ratio and effective radius of 0.098 g kg^{-1} and 8.19 μm, respectively. The reflectivity is of the same order as O_1, namely, -27.35 dBZ, but this observation contains far less drizzle ($N_T = 0.0088$ cm^{-3}, $l = 0.011$ g kg^{-1}, $r_e = 90.12$ μm), leading to a drizzle contribution to the total liquid water mixing ratio of only 10.24%. However, since the reflectivity is proportional to the sixth moment of the droplet spectrum, the contribution of the drizzle component (-4.40 dBZ) to the total reflectivity is still predominant (99.5%).

Practically all observations during the SOCEX campaigns are drizzle contaminated, leading to reflectivities that are dominated by the drizzle component of the particle spectrum. The contribution of the drizzle component to the total liquid water mixing ratio is significant (contribution larger than 10%) for 78% of all observations. The situation is similar but less serious for CLARE98. No drizzle was reported over Namibia.

Interestingly, the observations on the right-hand side of Fig. 1 appear to be constrained by the -20 dBZ isoline, not by their apparent height above cloud base, as would be expected if it were a random set of spectra. While it cannot be ruled out that the spectra were taken under highly selected, nonrandom conditions, it is more probable that it reflects the effect of drizzle on cloud depth. Several studies (Pincus and Baker 1994; Boers 1995) demonstrate that drizzle formation restricts cloud depth. In other words, deep clouds cannot be sustained in an environment of few droplets, as the few droplets would grow large and initiate the collision–coalescence process.

From a remote sensing perspective, it is useful to know a priori whether a cloud contains a significant amount of drizzle. As SOCEX data yield among the highest reflectivities expected of boundary layer clouds, Fig. 1 shows directly that the maximum reflectivity due to the nondrizzle component is around -20 dBZ, whereas the minimum reflectivity due to the drizzle component is about -10 dBZ. Thus, recalling that each data point represents one in situ observation averaged over an entire flight leg, on *average* there appears to be an evident jump of approximately 10 dBZ in reflectivity between a drizzle-contaminated and a drizzle-free droplet spectrum. Furthermore, inspection of the SOCEX datasets has shown that if the total reflectivity is below -5 dBZ, then the contribution to the total liquid water mixing ratio due to drizzle is negligible (5.4%, 0.0047 g kg^{-1} on average), and the total concentration of drizzle is low (0.0052 cm^{-3} on average). This delineation can be used to discriminate drizzling and nondrizzling clouds. It is interesting to note that Frisch et al. (1995) observed a similar delineation between drizzle and cloud droplets, albeit in their observations during the Atlantic Stratocumulus Transition Experiment (ASTEX) campaign -16 dBZ deliniation was more appropriate.

Clearly, the reflectivities isolines in Fig. 1 are only estimates based on the average of the gamma parameters (Table 1). To indicate the accuracy in the estimates of the reflectivity and the effective radius based on Fig. 1, given the liquid water mixing ratio and the total particle concentration, the standard deviations in the estimates of Z and r_e are computed as

TABLE 2. Accuracy of model-derived values of the effective radius and cloud reflectivity.

		FSSP		2DC	
	T	$\sigma(r_e)(\mu m)$	$\sigma(Z)(dBZ)$	$\sigma(r_e)(\mu m)$	$\sigma(Z)(dBZ)$
SOCEX1	30	0.39	1.04	28.13	2.88
SOCEX2	26	0.41	1.10	7.93	2.25
CLARE98	14	0.42	1.74	28.98	6.65

$$\sigma = \sqrt{\frac{\sum_i (X_i - O_i)^2}{T}}, \quad (12)$$

where X_i is the theoretically derived value of either Z or r_e [Eq. (10) and (11)] at coordinate $(N_{T,i}, l_i)$, where $N_{T,i}$ and l_i are the in situ–measured values. Here O_i is the calculated Z or r_e, based on the in situ observations, and T is the total number of observations. The resulting standard deviations are given in Table 2.

It shows that Fig. 1 can be used to predict r_e with an accuracy of approximately 5% in the nondrizzle case and roughly 30% in the drizzle case. The error of Z varies then from approximately 1.5 dB for the nondrizzle case to approximately 6 dB for drizzle. This error estimation is based on in situ observations done under different conditions and will likely also represent a realistic range of values of the β value for adiabatic conditions. This result demonstrates that this type of plot can be used as a universal guideline for reflectivity prediction.

3. Application to spaceborne radar

a. Cloud depth

The estimated parameters describing the gamma distribution are used in this section to construct a model of the reflectivity field and to simulate the expected spaceborne radar return. First, the performance of spaceborne radar with regards to the vertical structure of boundary layer clouds is considered. The impact of the large radar volume on the horizontal variation is discussed next with the aid of a fractal model, which simulates a cloud with a horizontal extent of 25 km × 25 km based on a mean total concentration, cloud thickness, and cloud top.

Inserting (8) into (11) yields

$$Z(z) = 64\psi_2\left(\frac{4\pi\rho_w}{3\rho_o}\right)^{-2}[(1-\beta)A_d]^2(z - z_b)^2 N_T^{-1} = C(z - z_b)^2 N_T^{-1}. \quad (13)$$

Thus, as mentioned before, the radar reflectivity varies quadratically with the height above cloud base for prescribed values of β and N_T. To simulate the expected return for a spaceborne radar, the actual reflectivity field is convoluted with the radar signal:

$$S(z) = S_i(z) \otimes Z(z) = \int S_i(z')Z(z - z')\, dz', \quad (14)$$

where S_i is the radar pulse shape function, which is assumed to be either a boxcar function or a Gaussian function; z' is a running parameter.

Figure 2 shows a vertical profile of Z (solid line), in accordance with Eq. (13) where $N_T = 50$ cm^{-3} (Figs. 2a,b) or 250 cm^{-3} (Figs. 2c,d), $\beta = 0.4$ and the cloud depth is 400 m. The dashed lines in the figures are the convoluted signals, and the dotted lines are the convoluted signals sampled at an interval of 500 m, which is the typical height resolution of a spaceborne radar, taking into account a radar sensitivity of −30 dBZ (WMO–WCPR 1994). Figures 2a and 2c show the convolution of the reflectivity field with a boxcar function and Figs. 2b and 2d result from convolution with a Gaussian function. Both radar signals have a pulse length of 500 m.

After convolution, the ''true'' reflectivity is ''smeared'' out in the vertical direction, consequently synthetically increasing the cloud thickness by 500 m. The signal for a boxcar function (Fig. 2a) produces a thicker cloud than for a Gaussian function (Fig. 2b). Similar results apply for $N_T = 250$ cm^{-3} except that the sampled cloud appears thinner (Fig. 2c,d) due to the lower reflectivities.

If the convoluted signal is next sampled at 500-m intervals, which would complete radar signal processing, the radar-detected cloud depth is greatly affected by the digitization level and the radar sensitivity. Let us assume a −30-dBZ sensitivity. Figures 2a–d each have a left side and a right side. The right-hand figures are similar to the left-side figure, with the mere difference that the digitization levels have been changed by an altitude of 250 m. The reason for showing this option is that the exact distance from the radar to the cloud is always unknown. The digitization level affects the returned radar signal in a complex manner. Focusing on Fig. 2a, it appears that the apparent cloud size after digitization in the right-hand figure is 500 m thinner than on the left, while the vertical location of the cloud is approximately equal in both figures. The reason is that digitization of the convoluted signal on the left will detect two points exceeding a sensitivity of −30 dBZ, but only one on the right side. Consequently, the apparent cloud thickness on the left is 1000 m, but only 500 m on the right. Compared to the actual thickness of 400 m, it is clear that large errors in sizing may occur in this manner. From Figs. 2b and 2c it is clear that the digitization level may also modify the apparent vertical position of the cloud by about 250 m. As is the case for Fig. 2d, the sampling level may even cause the cloud not to be seen at all.

b. Horizontal variations in cloud depth and microphysics

Figure 2 considers purely the impact of the convolution and the digitization on the vertical structure of

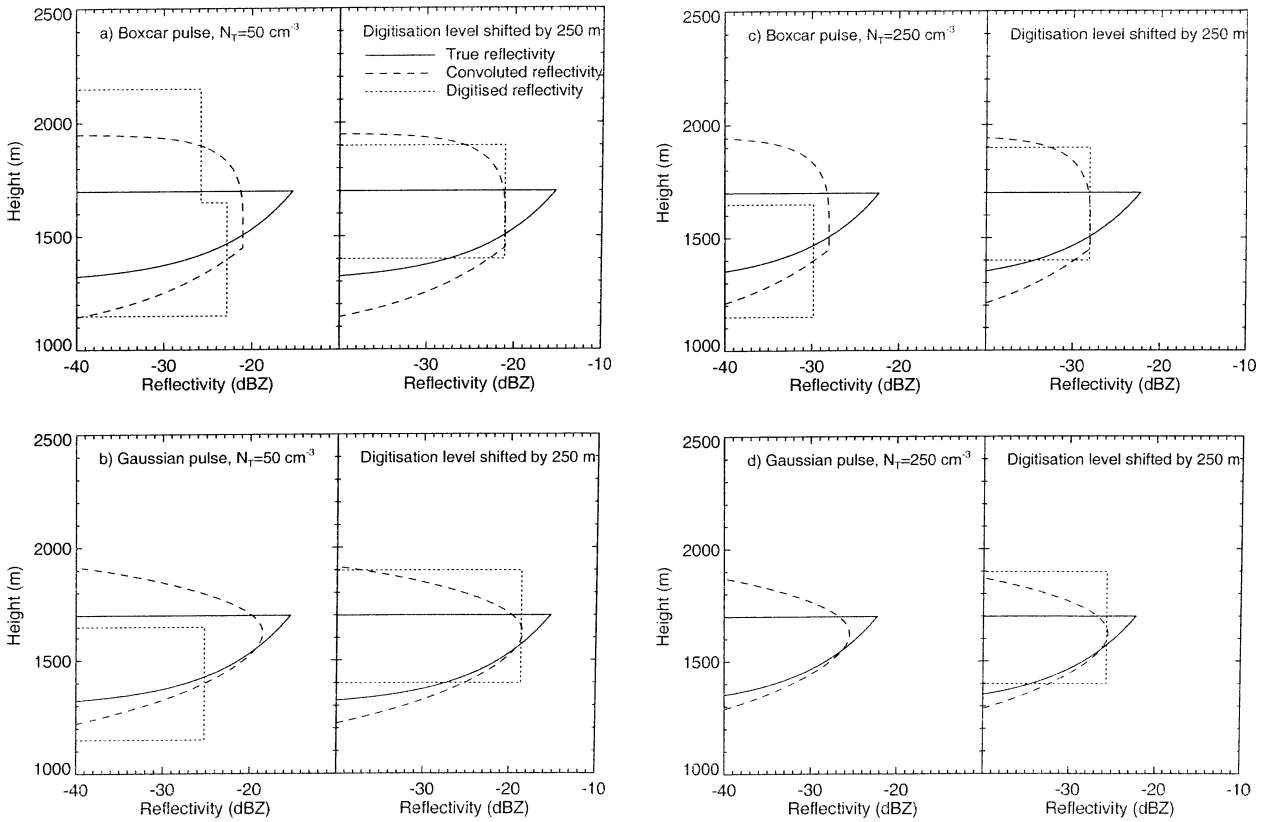

FIG. 2. The effect of convolution and digitization on cloud depth. (a) and (c) The signal processing using a boxcar radar pulse shape. (b) and (d) Processing using the Gaussian radar pulse shape. In (a) and (b) $N_T = 50$ cm^{-3}; in (c) and (d) $N_T = 250$ cm^{-3}. On the right side of each panel, the digitization level is shifted by 250 m to represent the uncertainty in absolute cloud height.

clouds. However, to simulate the expected radar return, an appropriate radar horizontal resolution has to be taken into account as well, which will have a great impact on the performance of the spaceborne radar to map the cloud stratification. To this end, a cloud with a horizontal extent of approximately 25 km $\times$ 25 km is simulated. This is accomplished with the aid of a bounded cascade model (Cahalan et al. 1994) and by considering the cloud top, the cloud thickness, and the total droplet concentration as scaling fractals. The purpose of using these fractals is not to construct a perfectly realistic cloud field, but to illustrate the effect of quasi-realistic fluctuations in controllable parameters.

The construction of the model will be explained in one dimension, which can then be simply expanded to a two-dimensional grid. First consider a uniform slab of atmosphere and a fixed value for, for instance, the liquid water content. The first cascade step is to divide the slab into two equal portions and to transfer a fraction f_1 of the total liquid from one-half of the segment to the other in a random direction. Two uniform slabs exist now, with an average liquid water content that is still equal to the total liquid. Next, each segment is again divided in two, and a fraction f_2 is randomly transferred within each newly formed segment, and so on. In order to reduce the variance at each cascade step, the fraction f_i is multiplied by a number smaller than 1:

$$f_i = f_{i-1}2^{-H}, \tag{15}$$

where i is the number of the cascade step, and $H > 0$. Various cloud parameters obey a $-5/3$ power law in the wavenumber spectrum of the cascade model (Davis et al. 1996; Marshak et al. 1997), which is obtained using $H \approx 0.33$. The bounded cascade model produces distribution functions that resemble a lognormal distribution. Other simulation models for the same intention could have been used. However, the bounded cascade model allows a manual adjustment of the variance-to-mean ratio of the distribution functions, which is convenient in the context of this study. The mean value and the standard deviations of the signals are given in Table 3 for each of the parameters.

Eight cascades are used, resulting in a grid of 256 $\times$ 256 pixels in the (x, y) plane. The radar footprint is taken as 1.4 km and one pixel is chosen to represent 100 m. Thus only a grid of 256 $\times$ 14 pixels is considered, yielding a cloud field of about 25 km $\times$ 1.4 km. The additional assumption that N_T is independent on height produces a 3D cloud model in the (x, y, z) plane. The effective radar footprint is assumed to be 4.0 km

TABLE 3. Mean values of cloud (micro)physical parameters in the fractal model.

	Mean	σ
Cloud top (m)	2000	439.4
Cloud depth (m)	400	70.1
N_T (cm^{-3})	300	100.2
N_T (cm^{-3})	50	16.7

$\times$ 1.4 km, which results from averaging the footprint over 0.3 s. It is assumed that the satellite's speed is 8 km s^{-1}, so that the effective radar footprint is obtained by averaging over an additional 26 pixels, after having averaged over the radar footprint (14 pixels). Numerous simulations were performed; only some examples are given.

In Fig. 3a the resulting reflectivity field in the (x, z) plane (averaged across-track) is given for $N_T = 50$ cm^{-3}. The large jumps in cloud height are included to simulate a worst-case scenario. However, observations from SOCEX confirm that the shown discontinuities do exist. Averaging the reflectivity across-track causes a smearing effect, similar to that produced by the convolution operation. Recalling that the mean cloud depth was originally 400 m, the reflectivity is now smeared over a height of roughly 600 m. The solid line represents the associated cloud top and cloud base, averaged across-track as well. Figure 3b displays the reflectivity after convolution with the boxcar function and shows that the amount of smearing caused by the convolution is approximately 400 m (Fig. 2). Notice that, although the reflectivity profile will be smeared out over a great vertical extent by the averaging and convolution operations, the mean value of the true cloud depth remains virtually unchanged (see also Fig. 4). The convoluted radar reflectivity, after averaging over the effective radar footprint, is given in Fig. 3c. A radar sensitivity of -30 dBZ is assumed. The solid line in Fig. 3c is the true cloud top and cloud base averaged over the same effective footprint, and the dashed line is the cloud top/base as ''seen'' by the radar. The along-track averaging modifies the reflectivity scene considerably, where the apparent cloud thickness reaches a maximum value of about 1.9 km. Figure 3d depicts the associated profiles of the optical depth and the droplet concentration (after averaging across-track). The optical depth ranges from 6 to 21, while the droplet concentration ranges from 30 to 60 cm^{-3}.

Figure 3e is the equivalent of Fig. 3c, but now for the larger droplet concentration of 300 cm^{-3}. Theoretically, the reflectivity decreases by about 7.8 dBZ when the total concentration increases by a factor of 6 [all other factors being equal, see Eq. (13) or Fig. 1]. According to Fig. 1 the reflectivity will exceed -30 dBZ when the height above cloud base is larger than 200 m (which was only about 70 m for $N_T = 50$ cm^{-3}). Consequently, the apparent cloud thickness is about 200 m thinner than the true thickness. Averaging the reflectivity across-track and by the convolution procedure, however, will compensate this effect by smearing out the reflectivity so as to obtain a cloud depth that is comparable to the true depth. Note however that there is now a sizable portion of the cloud that will not be detected by the radar at all.

For comparison with the estimated cloud thickness (h_{est}), the actual cloud thickness is defined in two ways. One method is to average the cloud thickness of the model over the effective footprint of the spaceborne radar, which generates the true cloud depth (h). The second method is to average the reflectivity of the model over the same effective footprint, and then define the cloud top and cloud base as the heights at which the reflectivity crosses the -30 dBZ threshold. The cloud depth that results from this method (h_2) is greatly affected by the averaging of the reflectivity over the effective radar footprint and is used to compare with h_{est} to gauge the impact of the convolution and the sampling operations on the retrieved cloud depth. The former method is only slightly affected by the averaging procedure, thus resulting in a much smaller value of the cloud depth when compared to the cloud thickness obtained using the latter method. This is illustrated in Fig. 4, which shows a vertical profile of reflectivity as the solid line (at the 11-km distance indicator in Fig. 3) after averaging over the effective radar footprint. The dashed line is the expected radar return and the total concentration is 50 cm^{-3}. The cloud thickness using the second method is 1630 m (top and base are at 2820 and 1190 m, respectively), while the true cloud thickness resulting from the first method is only 439 m (top and base are at 2086 m and 1647 m, respectively). Clearly, in Figs. 3c and 3e, h_2 will follow exactly the contours of the reflectivity profiles, and it is seen that the difference between h_2 and h_{est} (indicating the impact of the convolution and the sampling operation together) reaches a maximum value of approximately 500 m. When the averaging is taken into account as well (i.e., comparison with true cloud depth), the inaccuracy is much larger. The mean error is roughly 600 m, with a maximum error of about 1500 m. Although it should be recognized that the simulation shows a ''break'' in the cloud at 13 km over which the smoothing takes place (and thus represents a worse case scenario), these are very large errors and imply that the cloud-filled volume as estimated by the radar can on some occasions be vastly larger than present in reality.

The smearing effect depends on the radar sensitivity; the higher the sensitivity, the larger the smearing effect. If we take the cloud volume of the fractal model as reference, then a doubling occurs for a -40 dBZ threshold and 70% increase in apparant cloud volume for a -30 dBZ threshold. After the next processing step, namely sampling (digitization), the increase in volume referenced from the base value ranged from 20% to 100%. This large range is entirely dependent on the actual distance from the cloud to the radar, as explained

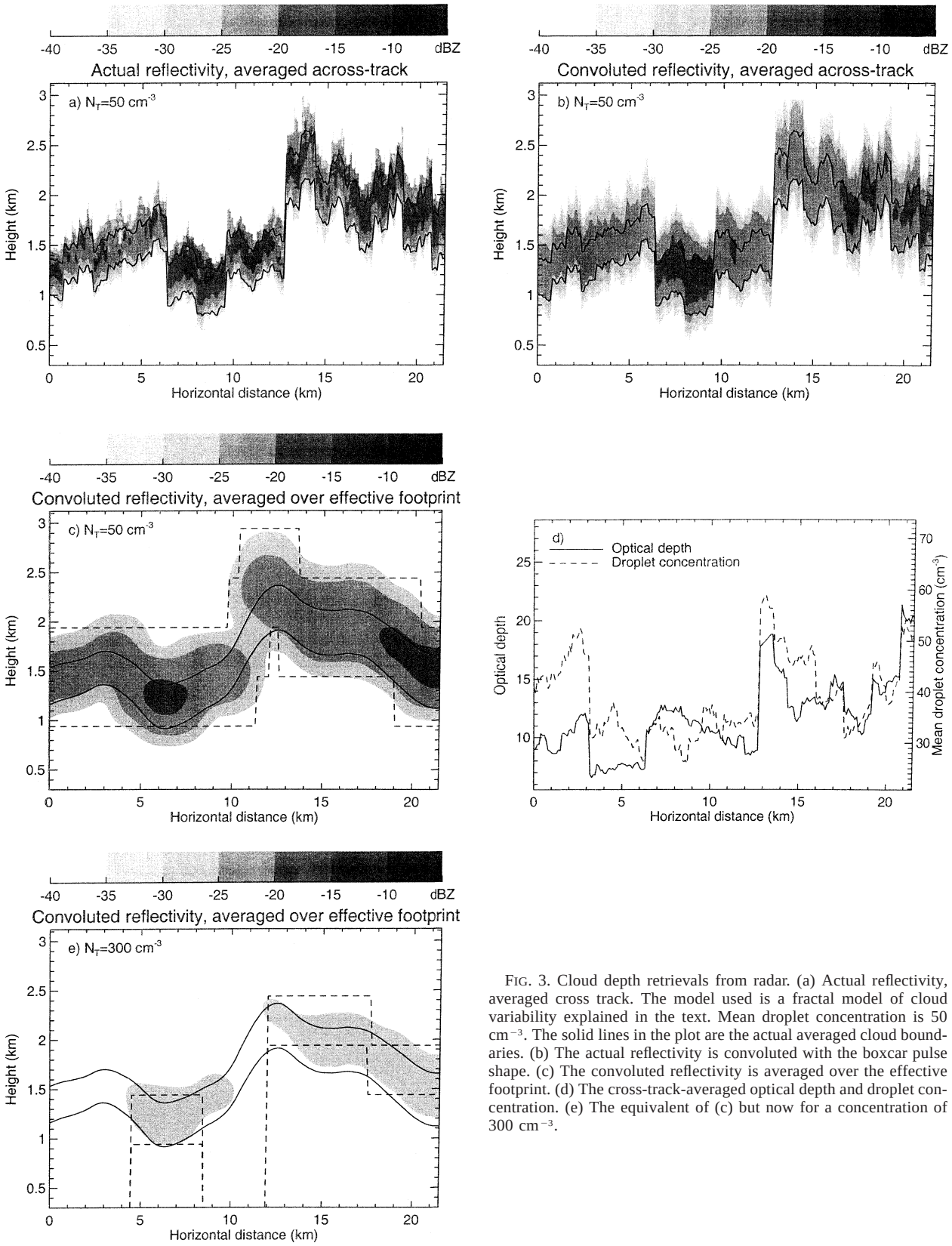

FIG. 3. Cloud depth retrievals from radar. (a) Actual reflectivity, averaged cross track. The model used is a fractal model of cloud variability explained in the text. Mean droplet concentration is 50 cm^{-3}. The solid lines in the plot are the actual averaged cloud boundaries. (b) The actual reflectivity is convoluted with the boxcar pulse shape. (c) The convoluted reflectivity is averaged over the effective footprint. (d) The cross-track-averaged optical depth and droplet concentration. (e) The equivalent of (c) but now for a concentration of 300 cm^{-3}.

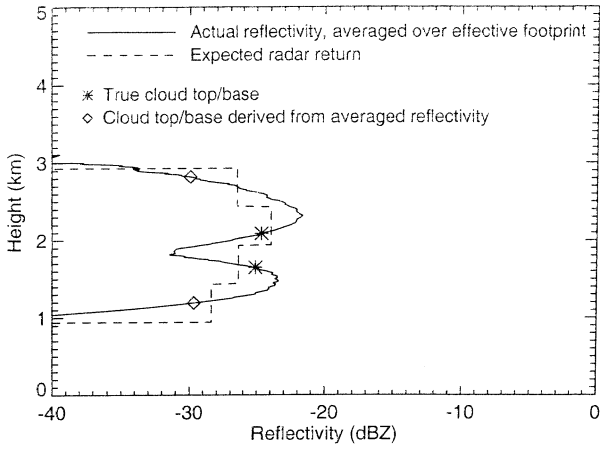

FIG. 4. Reflectivity averaged over footprint and the effect of convolution and digitization. Solid line is the reflectivity based on the cloud model averaged over the effective footprint of the radar. The two stars are averaged true cloud top and base, while the diamonds are the cloud top/base derived from the averaged unprocessed reflectivities. The broken line represents the radar reflectivity convoluted and digitized.

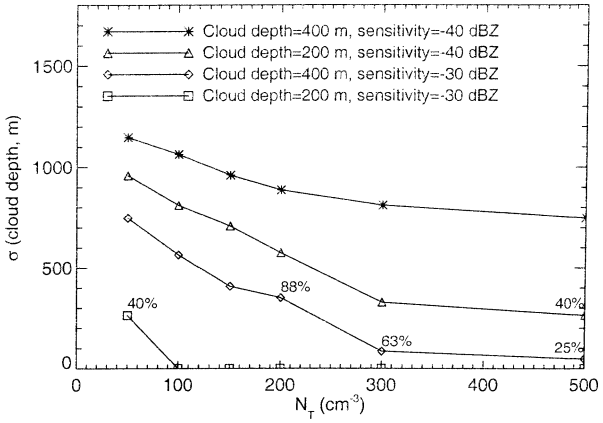

FIG. 5. The sensitivity of cloud depth determination on droplet number concentration. Sigma (σ) is the rms difference of model vs retrieved cloud depth. The percentages represent the cloud cover retrieved by the radar.

in Fig. 2. Clearly, the error made in estimating the cloud top and cloud base is smaller for higher droplet concentrations. However, this does not imply that the radar performance is better for higher droplet concentrations. It only means that two sources of error, namely low radar sensitivity and convolution, partly cancel each other out because, as mentioned, the reflectivity is inversely proportional to N_T. Consequently, for higher N_T, the amount of smearing caused by the convolution, averaging, and sampling is reduced.

Figure 5 displays the accuracy in the estimates of the cloud depths as a function of N_T. Four situations have been plotted. The asterisks and the diamonds represent the situations where the mean cloud thickness is 400 m, assuming a sensitivity of -40 and -30 dBZ, respectively. The cases where the mean cloud thickness is 200 m assuming a sensitivity of -40 and -30 dBZ are denoted by the triangles and the squares, respectively. The accuracy is computed as the standard deviation in the estimates of the cloud depth using Eq. (12), where X_i is the estimated cloud depth, and O_i is the true cloud depth. The percentages in the diagram reflect the amount of the actual cloud that is detected by the spaceborne radar, when different from 100%. It shows that a radar with a sensitivity of -30 dBZ will be unsuitable to detect clouds thinner than 200 m. When the cloud is at least 400 m, virtually all of the cloud will be detected using the same sensitivity, up to a total concentration of roughly 250 cm^{-3}. Radar that is capable of detecting a minimum reflectivity of -40 dBZ will be able to detect almost all clouds, which confirms the conclusions by Fox and Illingworth (1997a).

c. Retrieval of cloud liquid water and effective radius

Equations (10) and (11) suggest a straightforward way to obtain cloud droplet effective radius and liquid water in case the droplet concentration is known from other sources, because r_e is dependent on the 1/3 power of l, while Z is quadratic in l (see also Baedi et al. 2000). It is instructive to see the distribution of cloud droplet effective radius and liquid water retrieved after convolution of the radar pulse with the cloud reflectivity. Figure 6 shows the result that, while the range of liquid water and effective radius values sampled from the volume-averaged, -digitized, and -convoluted reflectivity is much smaller than the actually observed range of values, the mean values are not all that far from the truth. For $N_T = 50$ cm^{-3}, the model/retrieved values of Z, l, and r_e are $-18.09/-23.08$ dBZ, 0.20/0.18 g m^{-3}, and 11.75/10.58 μm, while for $N_T = 300$ cm^{-3} they are $-25.88/-28.27$ dBZ, 0.20/0.17 g m^{-3}, and 6.47/6.58 μm. However, the *modal* values of these parameters are substantially different from each other.

d. Drizzle

Thus far the contribution of the drizzle component of the particle spectrum has been neglected. Figure 7 shows how the drizzle component affects the vertical profiles of the effective radius, liquid water mixing ratio, and the reflectivity. The data are measured on 16 July 1993 during the SOCEX 1 campaign. On this day a uniform stratocumulus cloud over the Southern Ocean approximately 400 m thick was encountered, with drizzle showers below the cloud deck. The total droplet concentration was about 35 cm^{-3}. The asterisks in the figure contain only FSSP data, and the diamonds represent the merged FSSP and 2DC spectra. It shows that the drizzle contribution to the radar reflectivity completely overshadows the nondrizzle contribution. In the presence of drizzle, clouds will seem to extend to the lowest level where drizzle would be observed, which in many cases will almost be to the surface. Furthermore, the reflec-

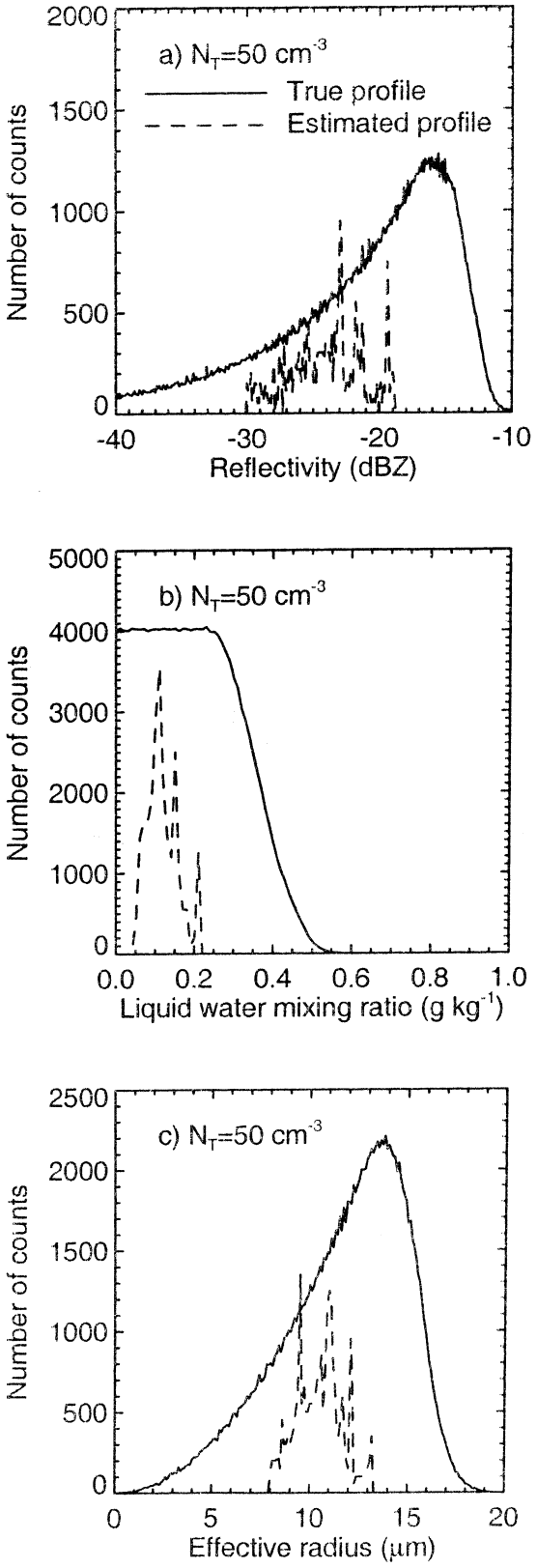

FIG. 6. Cloud reflectivity, liquid water, and effective radius as modeled (solid line) and retrieved (broken line).

tivity will not be related at all to the liquid water mixing ratio.

Boers et al. (1998) and Gerber (1996) demonstrated from observations that there is a threshold of the cloud droplet effective radius beyond which clouds will drizzle, although there appears to be some disagreement as to the exact value of the threshold. If we take a compromise value based on both studies ($r_e = 12$ μm) and compare this value against the value of r_e at cloud top for the model as shown in Figs. 3 and 4, then we find the entire cloud would be susceptible to drizzle if the droplet concentration was 50 cm^{-3}, and practically none of the cloud would be if the droplet concentration was 300 cm^{-3}. This means that in the drizzle regions the cloud radar reflectivity would be overwhelmed by reflectivity from droplets in and below cloud base, thus destroying the link between reflectivity, cloud depth, and liquid water content. Furthermore, it would mean that for the situation of $N_T = 50$ cm^{-3}, the cloud volume would be even more overestimated than it already is, as the drizzle signal from below cloud base would make it appear that clouds were present there as well.

Figure 1 can be used to broadly demarcate the clouds susceptible to drizzle. If we take a 12-μm isoline of effective radius as the boundary between clouds that drizzle and clouds that do not, then we find that this line follows approximately the following droplet concentration–cloud depth (i.e., height above cloud base) coordinates: (10 cm^{-3}, 60 m), (50 cm^{-3}, 300 m), (300 cm^{-3}, 1000 m). These numbers represent clouds with a varying optical thickness: from very thin to thick. Clearly, only very shallow marine nondrizzling clouds can be sustained for small concentrations, while at the high concentrations representing continental conditions, deep nondrizzling boundary layer clouds can be sustained. Of course, the precise location of the boundary is vague due to the fluctuations of the microphysical properties of individual cloud fields, and the uncertainty in precision of the threshold value of effective radius.

4. Discussion and conclusions

The detection of boundary layer water clouds is sensitive to the droplet concentration, radar pulse shape, digitization level, sensitivity, and averaging volume. Based on a universal diagram linking cloud liquid water, droplet concentration, and reflectivity we have shown that few boundary layer clouds will exceed a detection level of −20 dBZ. The universal diagram was based on a model of the microphysical parameters using truncated gamma distributions. The parameters describing this distribution were estimated using in situ probe data, and the diagram distinguishes the nondrizzle component of the particle spectra from the drizzle component. It appears that there is a significant gap in reflectivity between the nondrizzle and drizzle part of the spectra, implying that it could be straightforward to identify drizzle from nondrizzle regions. Cloud reflectivities ap-

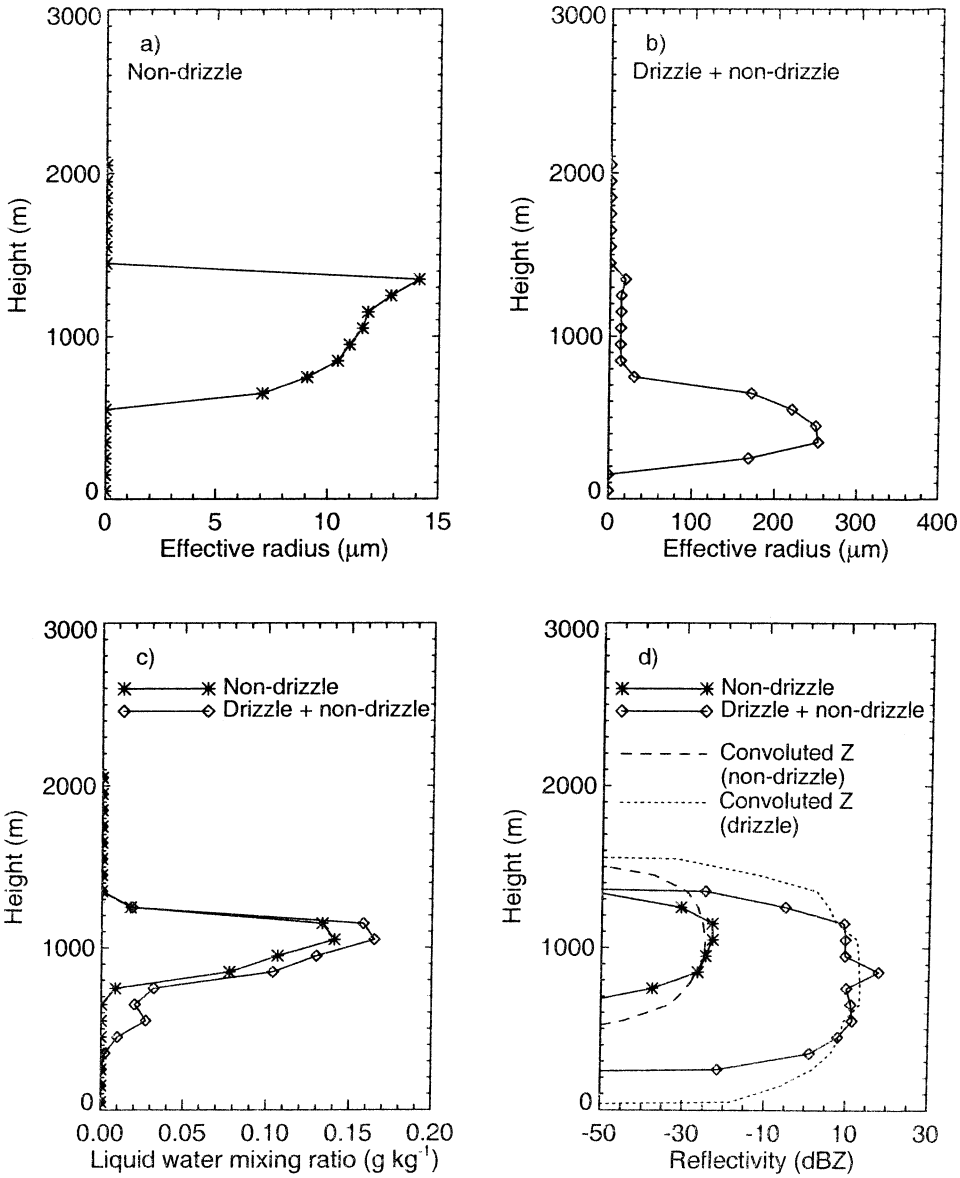

FIG. 7. The effect of drizzle on cloud reflectivity. (a) The effective radius for the nondrizzle portion of a cloud profile taken during SOCEX 1. (b) The effective radius for nondrizzle and drizzle combined. (c) The liquid water for drizzle and nondrizzle data. (d) The reflectivity for drizzle and nondrizzle data with and without convolution with the radar pulse shape.

pear not to exceed the −20 dBZ levels, even though this means that samples taken from clouds with few droplets must have been taken from shallower clouds than those with abundant droplets. It is suggested that this is caused by the depletion of cloud liquid water due to drizzle, which is responsible for cloud shrinkage. As many boundary clouds contain drizzle particles, detection of these clouds from space should not be too difficult.

The final cloud size estimate from radar is a complex function of several processes. The first step where the reflectivity is convoluted with the radar pulse shape will smear out the cloud spatially, but also decrease the observable reflectivity. In the next step, where the convoluted signal is digitized, only those points separated by the digitization separation (in our case 500 m) on the signal are selected that exceed the radar sensitivity. This can either increase, or decrease cloud size, or even will let a cloud vanish depending on the location of the cloud and the vertical coordinates of the digitization point on the radar signal.

An important conclusion of our work is that radar processing vastly increases the cloud-filled volume. Although sampling, sensitivity, and pulse length are important, an increase of 30%–100% in volume can be used as a guideline for typical boundary layer clouds.

This is of serious concern in studies that will use cloud radar to link cloud thickness, cloud fraction, and cloud liquid water to parameters relevant to radiative transfer problems. Also, the retrieval of parameters such as cloud liquid water content is hampered by the reflectivity distortions, as well as the locating of cloud water at places where it does not exist. A sizeable portion of marine clouds is susceptible to drizzle formation. In this study in situ data from different regions in the world were taken to simulate radar observations. There was a large contrast between the microphysical properties of clouds on the Northern and Southern Hemisphere due to differences in cloud condensation nuclei (CCN) concentrations. This may have a significant effect on the radiation balance and should be studied further.

In general, the results of this work rely on the number concentration being constant as a function of height. This is a reasonable assumption in closed stratocumulus clouds. In case of broken clouds, however, more intense mixing may occur, resulting in large variations on the number concentration with height. In the end, it is clear that radar data, taken by themselves, are insufficient to completely quantify cloud volume, microphysical, and optical parameters. It is only the combination of radar, lidar, and near-infrared radiometers that can enhance our knowledge of clouds. For instance, the lidar can be used to estimate the cloud top more accurately than what is feasible with the radar; this measurement can then be used to deconvolve the radar observation of the cloud and get a better estimate of the cloud thickness. Furthermore, the radar–lidar combination can help to classify drizzling and nondrizzling clouds (Baedi et al. 2000) and to retrieve microphysical cloud properties.

Acknowledgments. This study was carried out while R. Baedi held a student fellowship at CSIRO Atmospheric Research, Australia, and while R. Boers was employed there. R. Baedi's work was sponsored by the International Research Centre for Telecommunications–transmission and Radar, Delft University of Technology and by the VSB Funds Program of the Netherlands. The Namibia dataset was kindly provided by P. Francis of the Met Office. CLARE98 was funded by grants from the European Space Agency/ESTEC, Noordwijk, the Netherlands. R. Boers' work at CSIRO was sponsored in part by the Australian Greenhouse Office.

REFERENCES

Baedi, R. J. P., J. J. M. de Wit, H. W. J. Russchenberg, J. S. Erkelens, and J. P. V. P. Baptista, 2000: Estimating effective radius and liquid water content from radar and lidar based on the CLARE98 data set. *Phys. Chem. Earth B,* **25,** 1057–1062.

Betts, A. K., 1982: Cloud thermodynamic models in saturation point coordinates. *J. Atmos. Sci.,* **39,** 2182–2191.

Boers, R., 1995: Influence of seasonal variation in cloud condensation nuclei, drizzle, and solar radiation, on marine stratocumulus cloud optical depth. *Tellus,* **47B,** 578–586.

——, and R. M. Mitchell, 1994: Absorption feedback in stratocumulus clouds: Influence on cloud top albedo. *Tellus,* **46A,** 229–241.

——, J. B. Jensen, P. B. Krummel, and H. Gerber, 1996: Microphysical and radiative structure of wintertime stratocumulus clouds over the Southern Ocean. *Quart. J. Roy. Meteor. Soc.,* **122,** 1307–1339.

——, ——, and ——, 1998: Microphysical and radiative structure of marine stratocumulus clouds over the Southern Ocean: Summer results and seasonal differences. *Quart. J. Roy. Meteor. Soc.,* **124,** 151–168.

——, H. Russchenberg, J. Erkelens, V. Venema, A. van Lammeren, A. Apituley, and S. Jongen, 2000: Ground-based remote sensing of stratocumulus properties during CLARA, 1996. *J. Appl. Meteor.,* **39,** 169–181.

Cahalan, R. F., W. Ridgway, W. J. Wiscombe, T. L. Bell, and J. B. Snider, 1994: The albedo of fractal stratocumulus clouds. *J. Atmos. Sci.,* **51,** 2434–2455.

Clothiaux, E. E., M. A. Miller, B. A. Albrecht, T. P. Ackermann, J. Verlinde, D. M. Babb, R. M. Peters, and W. J. Syrett, 1995: An evaluation of a 94-GHz radar for remote sensing of cloud properties. *J. Atmos. Oceanic Technol.,* **12,** 201–229.

Davis, A., A. Marshak, W. J. Wiscombe, and R. F. Cahalan, 1996: Scale invariance of liquid water distributions in marine stratocumulus. Part I: Spectral properties and stationarity issues. *J. Atmos. Sci.,* **53,** 1538–1558.

ESA, 1999: *Int. Workshop Proc.: CLARE98 Cloud Lidar and Radar Experiment.* Noordwijk, Netherlands, ESTEC, WPP-170, 239 pp.

Fox, N., and A. Illingworth, 1997a: The potential of a spaceborne cloud radar for the detection of stratocumulus clouds. *J. Appl. Meteor.,* **36,** 676–687.

——, and ——, 1997b: The retrieval of stratocumulus cloud properties by ground-based radar. *J. Appl. Meteor.,* **36,** 485–492.

Frisch, A. S., C. W. Fairall, and J. B. Snider, 1995: Measurement of stratus cloud and drizzle parameters in ASTEX with a Ka-band Doppler radar and a microwave radiometer. *J. Atmos. Sci.,* **52,** 2788–2799.

Gerber, H., 1996: Microphysics of marine stratocumulus clouds with two drizzle modes. *J. Atmos. Sci.,* **53,** 1649–1662.

Han, Q., W. B. Rossow, and A. A. Lacis, 1994: Near-global survey of the effective droplet radii in liquid water clouds using ISCCP data. *J. Climate,* **7,** 465–497.

Lin, B., and W. B. Rossow, 1994: Observations of cloud liquid water path over the ocean: Optical and microwave sensing methods. *J. Geophys. Res.,* **99,** 20 907–20 927.

Marshak, A., A. Davis, W. J. Wiscombe, and R. F. Cahalan, 1997: Scale invariance in liquid water distributions in marine stratocumulus. Part II: Multifractal properties and intermittency issues. *J. Atmos. Sci.,* **54,** 1423–1444.

Pincus, R., and M. B. Baker, 1994: Effect of precipitation on the albedo susceptibility of clouds in the marine boundary layer. *Nature,* **372,** 250–252.

Rossow, W. B., and R. A. Schiffer, 1991: ISCCP cloud data products. *Bull. Amer. Meteor. Soc.,* **72,** 2–20.

——, and L. C. Garder, 1993: Validation of ISCCP cloud detection. *J. Climate,* **6,** 2370–2393.

WMO–WCPR, 1994: Utility and feasibility of a cloud profiling radar. Report of the GEWEX Topical Workshop. WMO Tech. Doc. 593, Pasedena, CA, 46 pp.